

## Atomic force microscopy based manipulation of graphene using dynamic plowing lithography

This article has been downloaded from IOPscience. Please scroll down to see the full text article.

2013 Nanotechnology 24 015303

(<http://iopscience.iop.org/0957-4484/24/1/015303>)

View [the table of contents for this issue](#), or go to the [journal homepage](#) for more

Download details:

IP Address: 147.91.1.43

The article was downloaded on 06/12/2012 at 11:06

Please note that [terms and conditions apply](#).

# Atomic force microscopy based manipulation of graphene using dynamic plowing lithography

Borislav Vasić<sup>1</sup>, Markus Kratzer<sup>2</sup>, Aleksandar Matković<sup>1</sup>,  
Andreas Nevasad<sup>2</sup>, Uroš Ralević<sup>1</sup>, Djordje Jovanović<sup>1</sup>,  
Christian Ganser<sup>2,3</sup>, Christian Teichert<sup>2</sup> and Radoš Gajić<sup>1</sup>

<sup>1</sup> Institute of Physics, University of Belgrade, Pregrevica 118, PO Box 68, 11080 Belgrade, Serbia

<sup>2</sup> Institute of Physics, Montanuniversität Leoben, Franz Josef Straße 18, A-8700 Leoben, Austria

<sup>3</sup> Christian Doppler Laboratory for Surface Chemical and Physical Fundamentals of Paper Strength, Graz University of Technology, Petersgasse 16/2, A-8010 Graz, Austria

E-mail: [bvasic@ipb.ac.rs](mailto:bvasic@ipb.ac.rs), [teichert@unileoben.ac.at](mailto:teichert@unileoben.ac.at) and [rgajic@ipb.ac.rs](mailto:rgajic@ipb.ac.rs)

Received 25 September 2012, in final form 30 October 2012

Published 5 December 2012

Online at [stacks.iop.org/Nano/24/015303](http://stacks.iop.org/Nano/24/015303)

## Abstract

Tapping mode atomic force microscopy (AFM) is employed for dynamic plowing lithography of exfoliated graphene on silicon dioxide substrates. The shape of the graphene sheet is determined by the movement of the vibrating AFM probe. There are two possibilities for lithography depending on the applied force. At moderate forces, the AFM tip only deforms the graphene and generates local strain of the order of 0.1%. For sufficiently large forces the AFM tip can hook graphene and then pull it, thus cutting the graphene along the direction of the tip motion. Electrical characterization by AFM based electric force microscopy, Kelvin probe force microscopy and conductive AFM allows us to distinguish between the truly separated islands and those still connected to the surrounding graphene.

 Online supplementary data available from [stacks.iop.org/Nano/24/015303/mmedia](http://stacks.iop.org/Nano/24/015303/mmedia)

(Some figures may appear in colour only in the online journal)

## 1. Introduction

Tailoring the geometry of graphene sheets is important for applications as well as for fundamental research. Cutting graphene into various nanostructures such as ribbons, dots and anti-dot lattices [1–6] enables an opening of its electronic band gap which is important for applications in nanoelectronics. On the other hand, mechanical deformation of graphene generates local strain which can strongly influence its electronic [7, 8], optical [9] and even magnetic properties [10, 11]. Both modifications could be realized by atomic force microscopy (AFM) based lithography [12, 13].

So far, AFM lithography has been used only for cutting graphene utilizing local anodic oxidation (LAO) based on either conductive AFM (C-AFM) [14–22] or scanning tunneling microscopy [23]. However, these techniques require broad ranges of the applied voltages, either metallic contacts

on the graphene flakes or conductive substrates, and increased humidity for LAO. In some cases, LAO could be initiated only at the edges of graphene [14]. Additionally, the process of making metallic contacts can lead to contamination, unintentional doping and shifting of the graphene Fermi level. In order to avoid the use of conductive parts in graphene lithography, a method based on a pure mechanical interaction is desirable. So far, only the scratching of graphene by an AFM tip operated in contact mode (static plowing) has been investigated [14, 24]. Problems with static plowing are uncontrollable crumbling or the undesired dragging, ripping and folding of large parts of the graphene flake along the silicon dioxide substrate by the AFM tip.

In this work we investigate the AFM based manipulation of graphene by dynamic plowing lithography (DPL). In contrast to the previously described AFM lithographic methods, which are solely dedicated to cutting, DPL enables

both types of mechanical manipulation: cutting or local deformation of graphene. In DPL, which was initially proposed for polymer and semiconductor structuring [25–28], the vibrating AFM tip is moved along the graphene in the so-called tapping mode. Opposite to the scratching in contact mode, the vibrating AFM tip is not in continuous contact with the graphene and the cantilever is essentially free from torsion, and thus not pushing/pulling the graphene laterally. This enables controllable deformation of graphene along arbitrarily shaped trenches without crumbling and dragging it along the substrate. We demonstrate that it is even possible to cut the graphene. However, in this case one cannot avoid pulling of the graphene by the AFM tip along the direction of tip motion, although the effect is less prominent than with static plowing. Electrical characterization of the cut graphene nanostructures was done by electric force microscopy (EFM), Kelvin probe force microscopy (KPFM) and C-AFM.

## 2. Experimental details

### 2.1. Sample preparation

Graphene samples were obtained by mechanical exfoliation of graphite [29] and transferred onto SiO<sub>2</sub>/Si substrates (the SiO<sub>2</sub> thickness was 300 nm). The samples were then visualized by optical microscopy whereas Raman spectroscopy was used in order to confirm the presence of single layer graphene. Metallic contacts were made using a simple home-made setup for photolithography using polymethylmethacrylate (PMMA) photoresist and a direct contact mask, followed by gold evaporation and lift off. We want to emphasize that the metallic contacts are not necessary for DPL but are needed for the subsequent electrical characterization by AFM based techniques.

### 2.2. AFM: scanning and tip calibration

All AFM measurements were performed at room temperature and under ambient conditions. AFM imaging and lithography were done using the NTEGRA Prima system from NT-MDT. In order to avoid significant tip damage during the lithography, we used V-shaped DCP20 cantilevers from NT-MDT with diamond coated tips. These cantilevers are sufficiently stiff with a typical force constant of 48 N m<sup>-1</sup> and a typical tip curvature radius of 50–70 nm. The calibration of the cantilevers was performed via the thermal noise method [30], employing an MFP 3D AFM system from Asylum Research. The applied method was originally developed for rectangular cantilever beams and enables calibration within an accuracy of 10% [31]. Due to the V-shape of the DCP20 cantilever, the real value of the force constant can be expected to be about 7% smaller than what is obtained from the thermal noise method [32]. Thus, the force constant was determined to be (59 ± 6) N m<sup>-1</sup>. For high-resolution AFM imaging of the patterned structures, we used NSG01 probes from NT-MDT with a much smaller tip curvature radius of about 6 nm and a typical force constant of 5 N m<sup>-1</sup>.

In order to convert the set-point values into real force values, we calibrated the forces by comparing the penetration depths obtained from classical force displacement indentation experiments and DPL using a procedure successfully applied to the DPL of polymer layers [33]. For the reader interested in the basics of dynamic AFM we refer to the supplementary information (available at [stacks.iop.org/Nano/24/015303/mmedia](http://stacks.iop.org/Nano/24/015303/mmedia)).

### 2.3. AFM dynamic plowing lithography

In order to increase the tip–sample interaction during dynamic plowing, the free-oscillation amplitude of the cantilever was increased by 10 times compared to ordinary scanning. Then, two amplitude set-point values were defined for lithography. The first value SP<sub>1</sub> was the same as for normal imaging and it was applied during the motion of the tip between lines aimed to be patterned. This prevented unwanted lithography in these areas of the tip motion. The second set-point SP<sub>2</sub> was 10–100 times smaller than SP<sub>1</sub>, meaning a significantly increased tip–sample interaction, and was applied for the patterning. Finally, fine tuning of SP<sub>2</sub> was done in order to obtain the desired depth of graphene deformation. Even though set-point values and set-point ratios in AFM are practical to work with, the authors are aware of the fact that these values do not impart an impression of the forces really acting between the tip and surface. Moreover, these values are generally not directly transferable between different AFM systems. Within this work, the corresponding force values are given where appropriate but otherwise we stay with the established set-point nomenclature. The velocity of the AFM tip motion during the lithography is 0.3–0.5 μm s<sup>-1</sup>.

### 2.4. AFM based electrical characterization

Figure 1 illustrates the setups for comprehensive AFM based electrical characterization. EFM was done utilizing the two-pass technique [34] for imaging of surface electric charges in graphene. We used the NTEGRA Prima AFM system and NT-MDT NSG01 tips with a conductive TiN coating. In the first pass, a topographic line was measured in tapping mode. Then, the tip was lifted by 30 nm and moved across the surface following the topographic contour from the first scan. During the second pass, the silicon substrate was grounded and a tip bias voltage,  $V_{DC}^{tip}$ , was applied between the substrate and the tip, as shown in figure 1(a). Electrostatic tip–sample interactions cause a phase lag which is recorded as a function of the position. Charging of graphene was done by bringing the graphene flake into contact with a biased tip for several minutes [35]. After that, EFM was used to measure the present surface charges.

KPFM was done using the two-pass technique [36] for imaging of the contact potential difference (CPD) between the graphene sample and the AFM tip. For these measurements, we employed an Asylum MFP-3D AFM and NT-MDT DCP11 probes with a nitrogen doped diamond coating. During the first pass, a topographic profile is acquired in tapping mode. In the second pass, the tip follows the

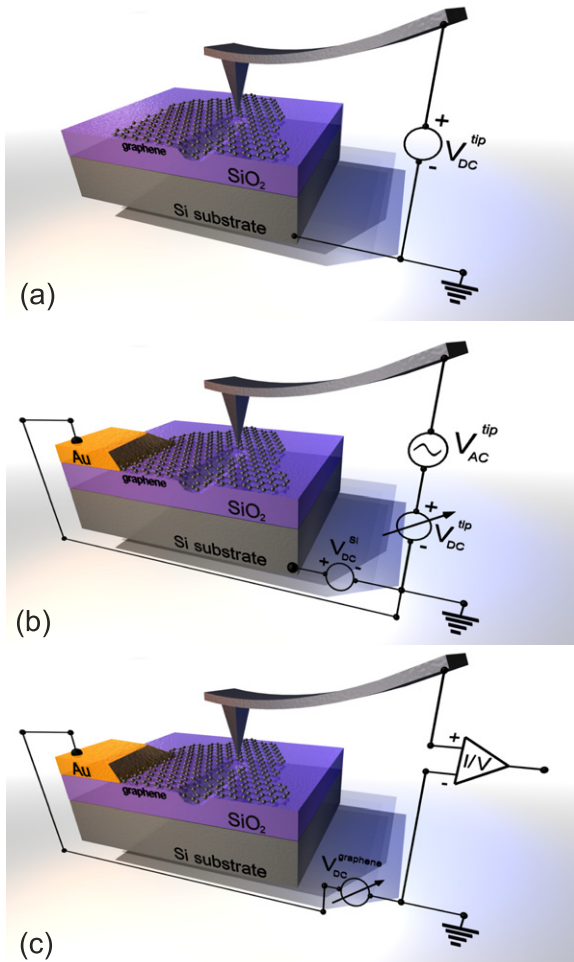


**Figure 1.** The experimental setups for the electrical characterization: (a) EFM, (b) KPFM, (c) C-AFM.

topographic profile at a preset lift height. During the second pass, the cantilever is electrically excited by the sum of a variable DC voltage  $V_{DC}^{tip}$ , and an AC voltage,  $V_{AC}^{tip}$ , with a frequency close to the cantilever resonance as depicted in figure 1(b).  $V_{DC}^{tip}$  is adjusted to nullify the force component at the frequency of  $V_{AC}^{tip}$ . The value of  $V_{DC}^{tip}$  is then equal to the CPD [37]. The tip was lifted by just a few nanometers in order to ensure that the tip-sample capacitance was dominant over the cantilever-sample capacitance. In our setup, we grounded the graphene and applied a bias voltage  $V_{DC}^{Si}$  to the silicon substrate. The substrate served as a back-gate in order to provide external control on the graphene surface potential.

For C-AFM, the conductive tip was scanned in contact mode across the biased sample. Topography and current were acquired simultaneously [38–41]. The C-AFM measurements of graphene were performed using the Asylum MFP-3D system and a Keithley 2636A dual source meter, as schematically shown in figure 1(c). For the measurements, DCP11 conductive diamond coated probes from NT-MDT with a typical force constant of  $11.5 \text{ N m}^{-1}$  were used. Since C-AFM operates in contact mode this is problematic for the measurement of graphene. The graphene can easily stick to the moving tip when scanning across the flake's edge,

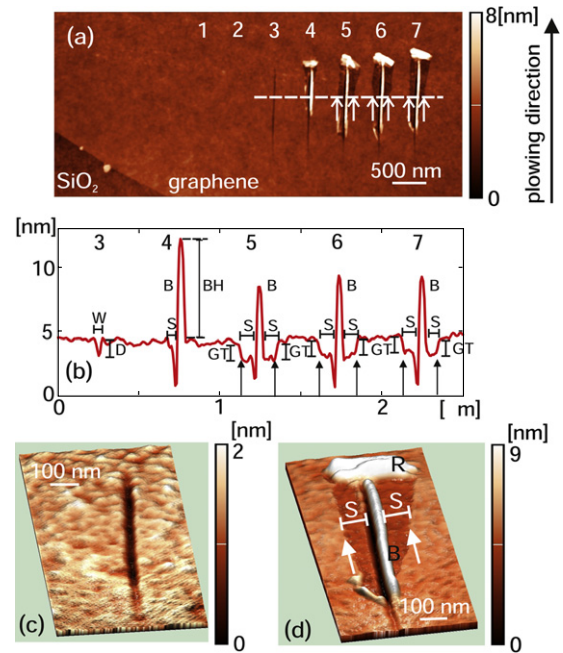


**Figure 2.** Morphological analysis of trenches made from the bottom to the top by DPL: (a) AFM topographic image, (b) the corresponding height profile along the dashed line in (a), (c) 3D AFM image of trench 3, (d) 3D AFM image of trench 7. The numbers 1–7 denote the trenches, the arrows denote the step-heights which represent the transitions from the substrate to graphene, and vice versa. Graphene thickness is denoted with GT, D is trench depth, W is trench width, B stands for bulges, BH stands for the bulge height, S denotes the smooth parts beside the trenches which correspond to the substrate. R denotes the graphene picked by the AFM tip, pulled and/or rolled and finally left at the end of the plowed trench.

ripping graphene parts off. Therefore, we started with local  $I$ - $V$  characterization, where the conductive AFM tip is put in a fixed position on the flake and a linear voltage ramp  $V_{DC}^{graphene}$  in the range of  $\pm 10 \text{ V}$  is applied to the graphene. The resulting current through the tip is then measured as a function of  $V_{DC}^{graphene}$ . Afterwards, the graphene is scanned in tapping mode to determine the flake's shape and position. From the latter measurement we could select a scan area on the flake for C-AFM in such a way that we did not risk scanning across its edges. Finally, a two-dimensional current map of the selected area was recorded at constant  $V_{DC}^{graphene}$ .

### 3. Results and discussion

In order to determine the proper  $SP_2$  value for DPL, seven parallel trenches were plowed with decreasing  $SP_2$ , where the following values of the relative set-point  $SP_R = SP_1/SP_2$  were applied: 10, 13.3, 16, 20, 26.6, 40 and 80. Figure 2(a) shows the AFM topographic image of the plowed trenches, whereas figure 2(b) shows a corresponding cross-sectional height profile. The  $SP_R$ s for trenches 1 and 2 were not large enough for noticeable deformation. Trench 3 is 1 nm deep and 40 nm wide and there were no bulges beside the trench. The corresponding force for the plowing of trench 3 was  $41 \mu\text{N}$ .

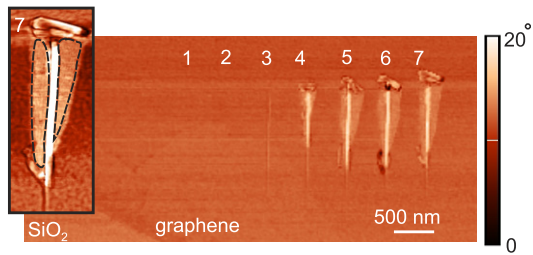


**Figure 3.** Phase image of the trenches from figure 2(a). The inset shows the phase image of trench 7. The dashed lines emphasize the observed phase contrast. This corresponds to the smooth parts at the sides of trench 7 in figures 2(a), (b) and (d). The white contrast of the bulges is mainly a topographic artifact.

A three-dimensional (3D) AFM image of trench 3 is shown in figure 2(c). It reveals smooth topographic contours indicating that the graphene and the substrate underneath were only deformed. The next four trenches (4–7) were 3–4 nm deep and 50 nm wide. The corresponding force for plowing these trenches was in the range of 59–68  $\mu\text{N}$ . The large bulges at the right side of the trenches were formed by material which was displaced during the plowing. Due to the irregularly shaped tip, the bulges are always formed at one side, leading to asymmetric profiles [27]. The bumps were 4–8 nm high. To the left and right of trenches 5, 6 and 7 in figure 2(b), there are smooth parts separated from the graphene surface by steps with heights of around 1 nm. This is better visualized in figure 2(d) where a 3D topographic image of trench 7 is shown. It seems that the smooth parts correspond to the substrate where graphene was removed by the AFM tip. The removed graphene was pulled and/or rolled and left at the top end of the trench where the tip finished plowing. The observed step-heights correspond to the transitions from the substrate to the graphene and vice versa.

Simultaneously with the topographic imaging, the phase lag of the cantilever oscillations was recorded. The phase imaging can give a material contrast of heterogeneous samples independently of topographic features [42]. The phase image of the trenches is depicted in figure 3. The phase contrast between the graphene flake and the  $\text{SiO}_2$  substrate is around  $1^\circ$ . At the left and right sides of trenches 5, 6 and 7, there is a phase contrast different from the rest of the graphene flake. This phase contrast corresponds exactly to the smooth parts beside the trenches in the topographic image in figure 2. This is highlighted in the inset of figure 3 where the phase image of trench 7 is shown. In order to check that the observed phase contrast was not a topographic artifact, the phase was measured in forward and backward scan directions. They were the same in both scans, thus confirming the material contrast. Therefore, we conclude that graphene was removed from the adjacent areas on both sides of trenches 5, 6 and 7 exposing the  $\text{SiO}_2$  substrate.

Applying the set-point parameters determined from the previous procedure, we fabricated closed circular trenches, thus forming individual graphene islands in order to investigate their electrical properties. An AFM topographic image of the two graphene islands prepared via DPL of one

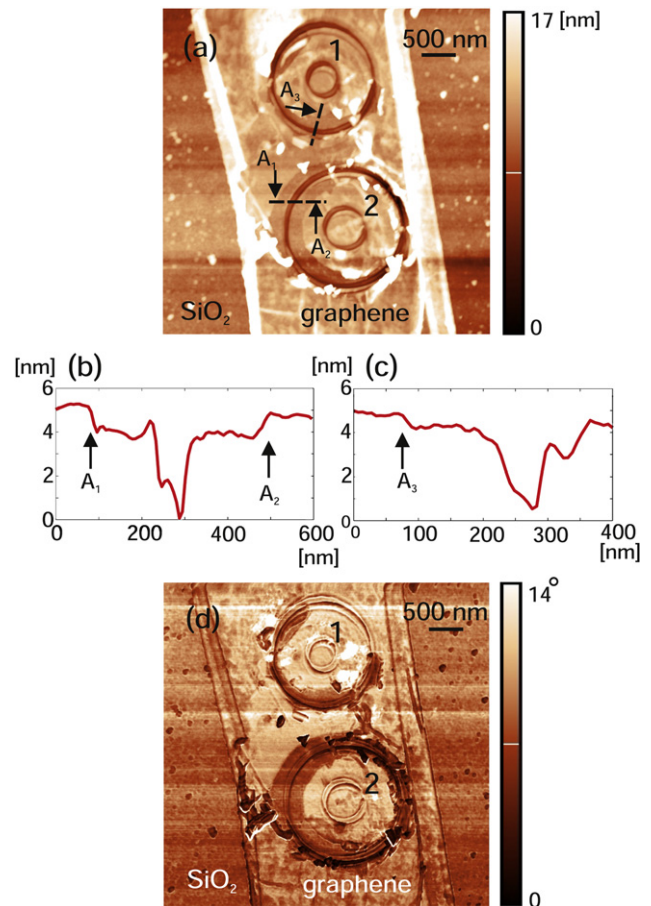


**Figure 4.** Graphene islands plowed with extremely high values of  $\text{SP}_R$ : (a) AFM topographic image, (b) and (c) the corresponding height profiles for the dashed lines in (a), and (d) the phase image. The islands are denoted with numbers 1 and 2. The bright, small dots in the image are photoresist residuals left from the metallic contact fabrication.

flake is shown in figure 4(a). The bright rims on both sides of the graphene flake are just its rolled-up edges. Both graphene islands consist of two concentric rings. Island 1 was plowed with  $\text{SP}_R = 80$  whereas island 2 was plowed with  $\text{SP}_R = 100$ . These two  $\text{SP}_R$  values were chosen in order to produce one island which is not completely separated from the flake in the former case, and one isolated island in the latter case. The depths of the resulting trenches were 3–4 nm, corresponding to forces in the range of 59–68  $\mu\text{N}$ . The cross-sectional height profiles across the outer trenches (figures 4(b) and (c)) show that at both sides of the trenches there are first smooth parts adjacent to 1 nm steps similar to the height profiles obtained for trenches 5–7 in figure 2(b). Again, the smooth parts correspond to the bare  $\text{SiO}_2$  substrate, whereas the steps indicate the transition to graphene. The corresponding phase image is depicted in figure 4(d). For both islands, parts with a phase contrast different from the graphene but similar to the substrate phase contrast can be found. Comparison with the corresponding topographic image reveals that these parts coincide with the graphene free areas. The phase image of island 1 suggests that it is still connected to the flake at the upper-right part. For island 2, the phase contrast is different

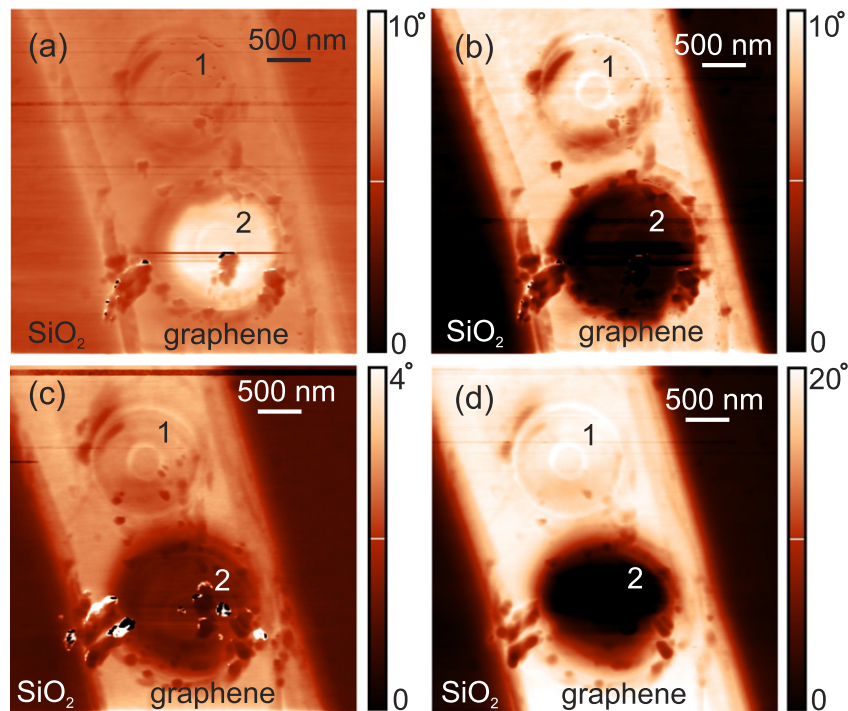


**Figure 5.** EFM images of the graphene islands: (a)  $V_{DC}^{tip} = -3$  V, (b)  $V_{DC}^{tip} = +3$  V, (c)  $V_{DC}^{tip} = +1$  V, before charging, and (d)  $V_{DC}^{tip} = +1$  V, after the charging with the AFM tip biased with  $-8$  V in the contact with island 1.

from the flake along the whole circumference of the island, indicating that it was completely isolated from the rest of the flake.

The islands have been further investigated using AFM based electrical characterization techniques. The EFM phase image of the graphene islands for tip bias voltages of  $V_{DC}^{tip} = -3$  V and  $V_{DC}^{tip} = +3$  V are shown in figures 5(a) and (b), respectively. For island 1, there is no difference in the EFM phase contrast between the island and the graphene. This means that they are not differently charged, indicating that the island is still connected to the surrounding graphene. However, island 2 shows a noticeable difference in the EFM phase contrast from the surrounding graphene. The phase contrast is reversed when the bias voltage  $V_{DC}^{tip}$  is changed from plus to minus confirming the electrostatic nature of the tip-island interaction. On island 2, positive (negative) phase shifts are measured for negative (positive)  $V_{DC}^{tip}$ , meaning that island 2 is positively charged compared to the rest of the graphene flake. This permanent storage of charges reveals that island 2 is really separated from the rest of the graphene [43].

In order to explore the charge transfer between the graphene islands and the flake, an attempt was made to charge the islands upon contact with the biased AFM tip. An EFM image of the graphene sample before charging and recorded at  $V_{DC}^{tip} = +1$  V is presented in figure 5(c). The phase contrast between island 2 and the rest of the graphene sample is around  $1.5^\circ$ . The tip was then brought into contact with the center of island 1 and biased at  $-8$  V for 10 min. Subsequently, the tip was lifted, switched to EFM mode and biased to the initial value of  $V_{DC}^{tip} = +1$  V. The EFM image after the charging is

shown in figure 5(d). The phase contrast between island 2 and the rest of the graphene has been increased to around  $24^\circ$ . The observed positive phase shift is the result of the additional negative charge of the graphene and the detection with the positive  $V_{DC}^{tip}$  which produced an additional attractive force component. The negative charges from the biased tip were transferred to island 1. Since it was electrically connected to the rest of the flake at its upper-right part, the charges were distributed over the graphene except in island 2 which was disconnected from the flake. This proves that the deformation of the graphene in the upper-right part of island 1 does not affect the charge transfer.

The KPFM results obtained for the circular graphene nanostructures are presented in figure 6(a) for both grounded silicon substrate and graphene flake (The images are rotated by  $90^\circ$  clockwise compared to the previously shown images, because a different AFM system was used for measurement.). KPFM reveals that the CPD for island 2 is larger compared to the rest of the graphene flake. This means that the island's work function is higher and its Fermi level is lower compared to the graphene flake so the island is positively charged with respect to the flake. This is in accordance with the EFM measurements. Next, we applied  $V_{DC}^{Si} = -5$  V and  $V_{DC}^{Si} = +5$  V to the silicon substrate which served as a back-gate. The CPD images for these two cases are shown in figures 6(b) and (c), respectively. The CPD in the grounded graphene flake changes due to the electric field effect from the back-gate: the negative (positive)  $V_{DC}^{Si}$  results in hole (electron) doping of the flake, which lowers (raises) its Fermi level, increases (decreases) its work function and thus increases (decreases) the CPD towards negative (positive) values. On the other hand, the

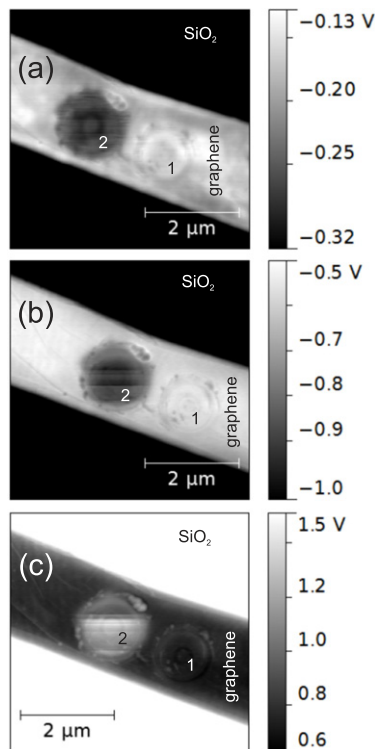


**Figure 6.** KPFM images of the graphene islands: (a)  $V_{DC}^{Si} = 0$  V, (b)  $V_{DC}^{Si} = -5$  V, (c)  $V_{DC}^{Si} = +5$  V. The range of the CPD scales was adjusted to improve the image contrast for the reader and does not resemble the full  $\pm 5$  V range.

CPD of island 2 just follows the bias voltage applied to the back-gate. Since this island was disconnected from the flake and from the ground, charging of the island by the electric field effect is not possible so island 2 was just polarized by  $V_{DC}^{Si}$ .

Current–voltage ( $I$ – $V$ ) curves were measured utilizing C-AFM in points within three different areas: island 1, island 2 and the graphene flake (the corresponding points are denoted in figure 7(a)). Measurements at each point were repeated several times in order to prove the reproducibility. The results are shown in figure 7(b). The current from island 2 was zero in the whole range of the applied voltage, confirming its electric isolation from the rest of the flake. The  $I$ – $V$  curves at two different positions on island 1 and the surrounding graphene flake were quite similar, confirming their electrical connection. This showed that under the applied conditions the DPL did not alter the electrical transport in island 1. The  $I$ – $V$  curves were quite symmetric and nonlinear, suggesting formation of a potential barrier between the AFM tip and the graphene sample. The deviation of the  $I$ – $V$  curve for point 3 for negative bias in figure 7(b) is most probably caused by a contact instability between the AFM tip and the surface and is therefore not related to the current transport within the graphene. After the measurement of the  $I$ – $V$  curves, two-dimensional (2D) current maps were recorded on the selected areas on both islands indicated in figure 7(a). For these measurements the graphene was biased by  $V_{DC}^{graphene} = -0.2$  V. The results for islands 1 and 2 are shown in figures

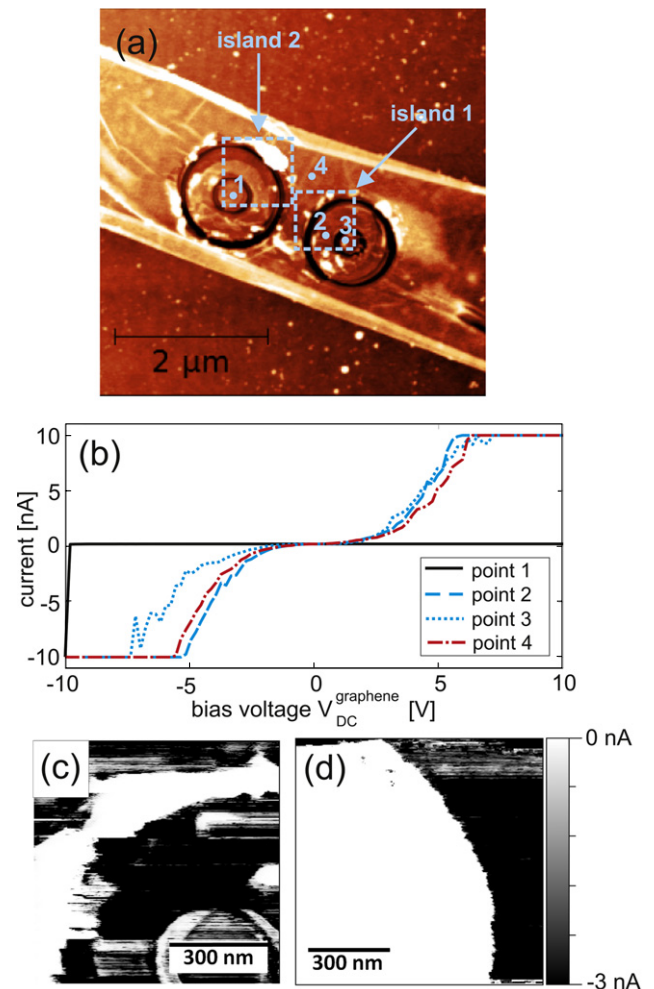


**Figure 7.** C-AFM results of graphene nanostructures: (a) tapping mode image to illustrate the location of  $I$ – $V$  curves and 2D C-AFM images, (b)  $I$ – $V$  curves, (c) 2D current maps for island 1, (d) 2D current maps for island 2 with 0.2 V bias applied to the graphene flake. The selected points for the  $I$ – $V$  curves are denoted with 1, 2, 3 and 4.

7(c) and (d), respectively. In accordance with the previous conclusions, the current is zero within island 2 and about  $-3$  nA for island 1.

The electrical analysis was also applied to other patterned graphene structures (not shown here) leading to comparable results. At an extremely low set-point  $SP_2$  for lithography it was possible to cut graphene, thus producing electrically isolated graphene islands. At the same time, the DPL with insufficiently high  $SP_R$  did not alter the electrical properties of the graphene as observed for island 1 whose electrical properties stayed the same as for the unpatterned graphene:  $I$ – $V$  characteristics as shown in figure 7(b), electric charge transfer as shown in figure 5(d) and the possibility of an electric field effect in figures 6(b) and (c). Since graphene is a mechanically very strong material [44], cutting requires very large mechanical forces and therefore low amplitude set-points. At extremely low set-points, the graphene sample is brought in very close proximity to the tip while the oscillations of the AFM probe are extremely small. In this case, dynamic plowing is rather like static plowing. During

DPL at low set-points, occasionally the AFM tip sticks to the graphene pulling it along the path of the tip movement thus ripping it off instead of cutting a trench. This could result in irregularly defined edges of the plowed structure. For this reason, the structures in figure 4 look more like polygons than circles. This might be a consequence of the fact that the cutting process mainly yields straight zig-zag or armchair edges which is an advantage since both edges are well defined not only in terms of crystallographic direction (no kinks or other defects) but also in terms of electrical properties.

Even though DPL exhibits qualitatively similar problems as known from static plowing the drawbacks are less pronounced. For static plowing the ‘cutting width’ has been reported to be up to  $1\ \mu\text{m}$  [14]. Smaller cutting widths were also reported but just for cuts along straight lines [24]. In addition, pronounced folding of large flake parts occurred when moving the tip in contact mode over the flake [14, 24]. Here, the circular islands were cut out from the middle of a graphene ribbon of just  $2\ \mu\text{m}$  width. The maximum cutting width in this case was 500 nm. Even though the DPL result is far from being perfect, the ribbon stayed essentially intact and the two structures are detached. Therefore, we believe that DPL application on graphene is useful when metallic contacts and/or substrates for LAO have to be avoided. Further, DPL is well applicable when the length scale of the edge irregularities is much smaller than the dimension of the graphene structure as we obtained here.

For a moderately low set-point  $SP_2$ , DPL can be used for local deformation of the graphene without cutting it. In figure 8, AFM topographic images of different geometric structures plowed with  $SP_R = 16$  are shown. The examples demonstrate that DPL can be used for patterns composed of straight trenches (figure 8(a)), straight and closed trenches (figure 8(b)), circular trenches (figure 8(c)) and even for arbitrary geometries such as the word ‘NANO’ (figure 8(d)). The topographic contours of the trenches are continuous and without abrupt steps and bulges, indicating that graphene was only deformed along the trenches. The deformation of graphene does not require such high mechanical forces as for cutting. Since there is no ripping, the formation of well defined geometric shapes within a graphene sheet is possible. The main benefit of DPL over static plowing is the reduction of lateral forces acting on the graphene sheet. In static plowing, friction forces with components normal to the cantilever’s long axis yield torsion of the cantilever, resulting in irregular edges of the plowed structures. In dynamic plowing, friction and torsion are avoided since the tip is vibrating and therefore is not in continuous contact with the surface. This enables plowing at any angle to the cantilever long axis with well defined edges of the patterned structures.

Dynamic plowing of graphene at a moderately low set-point  $SP_2$  enables controllable deformation of the graphene which is stretched along the bottom of the plowed trench. In this way it is possible to introduce local strain in graphene. The strain in the deformed graphene can be roughly estimated as  $(L - L_0)/L_0 \times 100\%$ , where  $L_0$  and  $L$  are the lengths of the graphene before and after the deformation [45]. The graphene length before deformation can be approximated as the trench

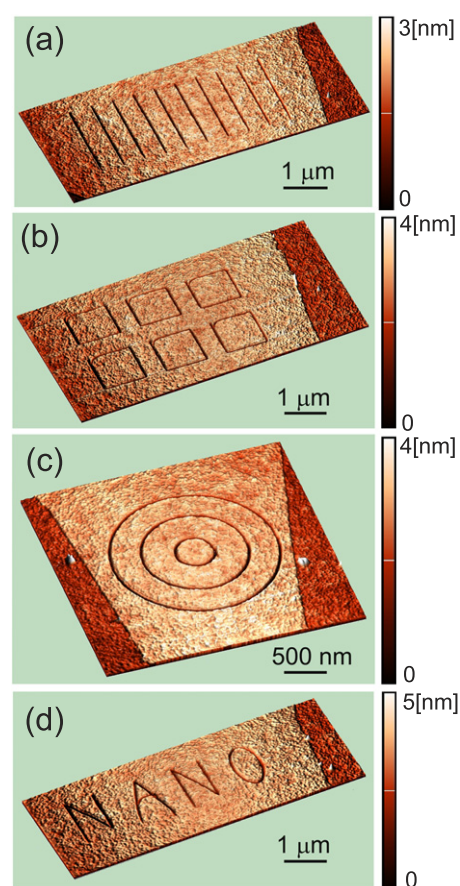


**Figure 8.** 3D AFM topographic images of structures fabricated by DPL in graphene: (a) lines, (b) squares, (c) circles, (d) the word ‘NANO’.

width, whereas the graphene length after the deformation can be approximated as the circumference of the trench as sketched in figure 9. From the recorded AFM topographic images in figure 8, we could determine the values for  $L_0$  and  $L$ . For the average trench width of 50 nm and a trench depth in the range of 1–2 nm (the corresponding deformation force was in the range of 41–50  $\mu\text{N}$ ), the estimated tensile strain is in the range of 0.08% to 0.32%. An increase of strain can be achieved via the creation of deeper and narrower trenches by employing sharper AFM tips.

Scanning electron microscopy images (not shown here) of the used probes reveal little tip blunting. However, after extensive DPL at very low set-points pronounced degradation can occur. In general, a degraded tip demands far higher contact forces in order to cut/deform the graphene. Higher contact forces can simply be provided by lowering the set-point and/or increasing of the free-oscillation amplitude. Practically, a significant change of the plowing parameters is only necessary for strongly degraded tips. The enlarged tip radius sets limits to the trench width and therefore limits the achievable strain in the graphene. Strongly degraded tips might also lead to increased sticking of the graphene to the tip during DPL, resulting in enhanced graphene ripping. Such problems due to tip wear can be avoided by occasional evaluation of the condition of the tip, which can

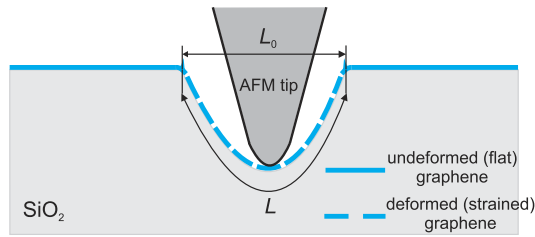


**Figure 9.** Sketch of the graphene locally strained by the AFM tip.

be accomplished with reasonable expenditure of time using a tip characterizer [46].

#### 4. Conclusion

DPL was applied to graphene the first time and extends the possibilities for AFM based manipulation of graphene due to its twofold action: (1) cutting of graphene or (2) graphene deformation and generation of local strain. For the AFM probes used in this study (DCP20: diamond coated, force constant  $k = 59 \pm 6 \text{ N m}^{-1}$ , tip curvature radius 50–70 nm), cutting of graphene requires extremely low values of  $\text{SP}_2$  corresponding to forces above  $60 \mu\text{N}$ . Under these conditions, the AFM cantilever oscillations are greatly suppressed and dynamic plowing is similar to static plowing (scratching). Sometimes, the graphene sticks to the tip and is practically torn, resulting in irregular edges of the carved structures. However, these drawbacks are less pronounced than with static plowing, enabling the cutting of curved shapes even in narrow ribbons. Therefore, the use of DPL for the fabrication of graphene nanostructures is limited, but it can serve as a useful tool for the fabrication of graphene structures where the influence of the edge irregularities can be neglected. EFM, KPFM and C-AFM proved the electrical isolation of a circular island which is laterally disconnected from the rest of the graphene flake by DPL. The electrical properties of islands, where the separation by DPL was incomplete, were kept the same as in the rest of the flake, indicating that the DPL process did not alter the local electrical properties of the patterned graphene structure.

At moderately low  $\text{SP}_2$  corresponding to forces below  $50 \mu\text{N}$ , the graphene was only deformed without cutting. This process is well controlled thus giving a new tool for the generation of local strain in graphene. For the typical widths and depths of the plowed trenches, the generated local strain in graphene has been estimated to be about 0.1%. In contrast to scratching (static plowing) where the occurring cantilever torsion limits the plowing directions to rather small angles with respect to the cantilever's long axis, the vibrating AFM cantilever in DPL does not suffer from torsion during plowing. Therefore, the plowing direction in DPL is not restricted to small scan angles (with respect to the cantilever's long axis). This allows the fabrication of regular trenches with well defined edges irrespective of their orientation or shape. The use of sharper AFM tips will result in narrower trenches, thus increasing the resolution of the lithography and/or generating larger local strain. There is still space for further optimization

of the method for increased control of the plowing and higher resolution.

Strain in graphene results in a shifting of the phonon frequencies which was observed by Raman spectroscopy [45, 47]. The spatial resolution to measure sub-100 nm structures is provided by tip-enhanced Raman spectroscopy which has already been applied for the measurement of strain in carbon nanotubes and  $\text{C}_{60}$  molecules which were deformed by AFM nanoindentation [48]. Therefore, we propose that tip-enhanced Raman spectroscopy is the proper tool to measure strain in plowed graphene trenches in the future.

#### Acknowledgment

This work was supported by the Serbian Ministry of Science under project no. OI171005, by the European Community's 7th Framework Programme under grant agreement no. 228637 NIM NIL ([www.nimnil.org](http://www.nimnil.org)), by the Austrian Science Foundation under project no. P19636-N20 and partly by FFG Austria under Bridge project no. 824890. We would like to thank Kartik Pondicherry, Department of Mechanical Engineering, Montanuniversität Leoben, for performing the scanning electron microscopy characterization of the AFM probes.

#### References

- [1] Han M Y, Özyilmaz B, Zhang Y and Kim P 2007 Energy band-gap engineering of graphene nanoribbons *Phys. Rev. Lett.* **98** 206805
- [2] Stampfer C, Güttinger J, Hellmüller S, Molitor F, Ensslin K and Ihn T 2009 Energy gaps in etched graphene nanoribbons *Phys. Rev. Lett.* **102** 056403
- [3] Pedersen T G, Flindt C, Pedersen J, Jauho A-P, Mortensen N A and Pedersen K 2008 Optical properties of graphene antidot lattices *Phys. Rev. B* **77** 245431
- [4] Kim M, Safron N S, Han E, Arnold M S and Gopalan P 2010 Fabrication and characterization of large-area, semiconducting nanoporated graphene materials *Nano Lett.* **10** 1125
- [5] Liang X, Jung Y-S, Wu S, Ismach A, Olynick D L, Cabrini S and Bokor J 2010 Formation of bandgap and subbands in graphene nanomeshes with sub-10 nm ribbon width fabricated via nanoimprint lithography *Nano Lett.* **10** 2454
- [6] Bai J, Zhong X, Jiang S, Huang Y and Duan X 2010 Graphene nanomesh *Nat. Nanotechnol.* **5** 190
- [7] Pereira V M and Castro Neto A H 2009 Strain engineering of graphene's electronic structure *Phys. Rev. Lett.* **103** 046801
- [8] Castro Neto A H and Novoselov K 2011 Two-dimensional crystals: beyond graphene *Mater. Express* **1** 10
- [9] Pereira V M, Ribeiro R M, Peres N M R and Castro Neto A H 2010 Optical properties of strained graphene *Europhys. Lett.* **92** 67001
- [10] Guinea F, Katsnelson M I and Geim A K 2010 Energy gaps and a zero-field quantum hall effect in graphene by strain engineering *Nat. Phys.* **6** 30
- [11] Levy N, Burke S A, Meaker K L, Panlasigui M, Zettl A, Guinea F, Castro Neto A H and Crommie M F 2010 Strain-induced pseudo-magnetic fields greater than 300 T in graphene nanobubbles *Science* **329** 544
- [12] Xie X N, Chung H J, Sow C H and Wee A T S 2006 Nanoscale materials patterning and engineering by atomic force microscopy nanolithography *Mater. Sci. Eng. R* **54** 1

- [13] Rosa L G and Liang J 2009 Atomic force microscope nanolithography: dip-pen, nanoshaving, nanografting, tapping mode, electrochemical and thermal nanolithography *J. Phys. Condens. Matter* **21** 483001
- [14] Giesbers A J M, Zeitler U, Neubeck S, Freitag F, Novoselov K S and Maan J C 2008 Nanolithography and manipulation of graphene using an atomic force microscope *Solid State Commun.* **147** 366
- [15] Weng L, Zhang L, Chen Y P and Rokhinson L P 2008 Atomic force microscope local oxidation nanolithography of graphene *Appl. Phys. Lett.* **93** 093107
- [16] Masubuchi S, Ono M, Yoshida K, Hirakawa K and Machida T 2009 Fabrication of graphene nanoribbon by local anodic oxidation lithography using atomic force microscope *Appl. Phys. Lett.* **94** 082107
- [17] Masubuchi S, Arai M and Machida T 2011 Atomic force microscopy based tunable local anodic oxidation of graphene *Nano Lett.* **11** 4542
- [18] Neubeck S, Freitag F, Yang R and Novoselov K S 2010 Scanning probe lithography on graphene *Phys. Status Solidi b* **247** 2904
- [19] Puddy R K, Scard P H, Tyndall D, Connolly M R, Smith C G, Jones G A C, Lombardo A, Ferrari A C and Buitelaar M R 2011 Atomic force microscope nanolithography of graphene: cuts, pseudocuts, and tip current measurements *Appl. Phys. Lett.* **98** 133120
- [20] Byun I-S et al 2011 Nanoscale lithography on monolayer graphene using hydrogenation and oxidation *ACS Nano* **5** 6417
- [21] Rius G, Camara N, Godignon P, Perez-Murano F and Mestres N 2009 Nanostructuring of epitaxial graphene layers on SiC by means of field-induced atomic force microscopy modification *J. Vac. Sci. Technol. B* **27** 3149
- [22] Alaboson J M P, Wang Q H, Kellar J A, Park J, Elam J W, Pellin M J and Hersam M C 2011 Conductive atomic force microscope nanopatterning of epitaxial graphene on SiC(0001) in ambient conditions *Adv. Mater.* **23** 2181
- [23] Tapasztó L, Dobrik G, Lambin Ph and Biro L P 2008 Tailoring the atomic structure of graphene nanoribbons by scanning tunnelling microscope lithography *Nat. Nano.* **3** 397
- [24] Eilers S and Rabe J P 2009 Manipulation of graphene within a scanning force microscope *Phys. Status Solidi. B* **246** 2527
- [25] Wendel M, Kuhn S, Lorenz H, Kotthaus J P and Holland M 1994 Nanolithography with an atomic force microscope for integrated fabrication of quantum electronic devices *Appl. Phys. Lett.* **65** 1775
- [26] Klehn B and Kunze U 1999 Nanolithography with an atomic force microscope by means of vector-scan controlled dynamic plowing *J. Appl. Phys.* **85** 3897
- [27] Kunze U 2002 Invited review nanoscale devices fabricated by dynamic ploughing with an atomic force microscope *Superlattices Microstruct.* **31** 3
- [28] Heyde M, Rademann K, Cappella, Geuss M, Sturm H, Spangenberg T and Niehus H 2001 Dynamic plowing nanolithography on polymethylmethacrylate using an atomic force microscope *Rev. Sci. Instrum.* **72** 136
- [29] Novoselov K S, Jiang D, Schedin F, Booth T J, Khotkevich V V, Morozov S V and Geim A K 2005 Two-dimensional atomic crystals *Proc. Natl. Acad. Sci. USA* **102** 10451
- [30] Hutter J L and Bechhoefer J 1993 Calibration of atomic-force microscope tips *Rev. Sci. Instrum.* **64** 1868
- [31] Matei G A, Thoreson E J, Pratt J R, Newell D B and Burnham N A 2006 Precision and accuracy of thermal calibration of atomic force microscopy cantilevers *Rev. Sci. Instrum.* **77** 083703
- [32] Stark R W, Drobek T and Heckl W M 2001 Thermomechanical noise of a free v-shaped cantilever for atomic-force microscopy *Ultramicroscopy* **86** 207
- [33] Cappella B and Sturm H 2002 Comparison between dynamic plowing lithography and nanoindentation methods *J. Appl. Phys.* **91** 506
- [34] Datta S S, Strachan D R, Mele E J and Johnson A T C 2009 Surface potentials and layer charge distributions in few-layer graphene films *Nano Lett.* **9** 7
- [35] Verdaguer A, Cardellach M, Segura J J, Sacha G M, Moser J, Zdrojek M, Bachtold A and Fraxedas J 2009 Charging and discharging of graphene in ambient conditions studied with scanning probe microscopy *Appl. Phys. Lett.* **94** 233105
- [36] Yu Y-J, Zhao Y, Ryu S, Brus L E, Kim K S and Kim P 2009 Tuning the graphene work function by electric field effect *Nano Lett.* **9** 3430
- [37] Nonnenmacher M, O'Boyle M P and Wickramasinghe H K 1991 Kelvin probe force microscopy *Appl. Phys. Lett.* **58** 2921
- [38] Teichert C and Beinik I 2011 Conductive atomic-force microscopy investigation of nanostructures in microelectronics *Scanning Probe Microscopy in Nanoscience and Nanotechnology* vol 2, ed B Bhushan (Berlin: Springer) pp 691–721
- [39] O'Shea S J, Atta R M, Murrell M P and Welland M E 1995 Conducting atomic force microscopy study of silicon dioxide breakdown *J. Vac. Sci. Technol. B* **13** 1945
- [40] Olbrich A, Ebersberger B and Boit C 1998 Conducting atomic force microscopy for nanoscale electrical characterization of thin SiO<sub>2</sub> *Appl. Phys. Lett.* **73** 3114
- [41] Kremmer S, Teichert C, Pischler E, Gold H, Kuchar F and Schatzmayr M 2002 Characterization of silicon gate oxides by conducting atomic force microscopy *Surf. Interface Anal.* **33** 168
- [42] Martínez N F and García R 2006 Measuring phase shifts and energy dissipation with amplitude modulation atomic force microscopy *Nanotechnology* **17** S167
- [43] Kurra N, Prakash G, Basavaraja S, Fisher T S, Kulkarni G U and Reifengerger R G 2011 Charge storage in mesoscopic graphitic islands fabricated using AFM bias lithography *Nanotechnology* **22** 245302
- [44] Lee C, Wei X, Kysar J W and Hone J 2008 Measurement of the elastic properties and intrinsic strength of monolayer graphene *Science* **321** 385
- [45] Ni Z H, Yu T, Lu Y H, Wang Y Y, Feng Y P and Shen Z X 2008 Uniaxial strain on graphene: Raman spectroscopy study and band-gap opening *ACS Nano* **2** 2301
- [46] Villarrubia J S 1994 Morphological estimation of tip geometry for scanned probe microscopy *Surf. Sci.* **321** 287
- [47] Mohiuddin T M G et al 2009 Uniaxial strain in graphene by Raman spectroscopy: G Peak splitting, Gruneisen parameters, and sample orientation *Phys. Rev. B* **79** 205433
- [48] Yano T, Unouye Y and Kawata S 2006 Nanoscale uniaxial pressure effect of a carbon nanotube bundle on tip-enhanced near-field Raman spectra *Nano Lett.* **6** 1269